Supporting Information

Ingaramo et al. 10.1073/pnas.1314447111

SI Text

Two-Photon Multifocal Structured Illumination Microscopy Implementation

Implementation of two-photon multifocal structured illumination microscopy implementation (2P-MSIM) required substantial modifications to the previous MSIM design (1). The original MSIM used a digital micromirror device which works well in producing evenly spaced sparse excitation foci. However, as only a tiny fraction of the mirrors illuminate the sample at any instant, this approach is extremely inefficient at delivering excitation light to the sample. As discussed previously (1), a design similar to a swept-field microscope would be more efficient and perhaps even necessary for multiphoton excitation in MSIM, where signal is proportional to the peak intensity squared. Several configurations for multifocal multiphoton instruments have been reported. One option would have been to devise a multiplexing unit to split the beam into many beamlets which could be scanned over the sample (2–4), similar to the commercial TriM scope (LaVision BioTec). In fact, a multiphoton SIM technique was published using a TriM microscope in which multiline scans were used to make striped illumination patterns in the sample (5). A second multifocal approach would be to use a microlens array either in a spinning disk (6–12) or stationary configuration (13, 14). We opted for a simple design which collects images in widefield mode and allows precise control over the pattern and position of excitation spots using a stationary microlens array to generate the sparse foci illumination (Fig. S1). Our initial design relied on the precise orientation of the microlens array and precise spacing of the excitation spots in conjunction with a single galvanometer to control the excitation beam angles. This allowed single-axis translation of the illumination spots over the entire sample to produce as uniform illumination as possible. However, we found a 2D galvanometric scanner as used in a previous multifocal multiphoton microscope (13) was more simple to implement and alleviated the need for precise spot spacing and microlens array orientation to produce uniform illumination. An additional correction for overlapping coverage was implemented in the MSIM analysis software (*Methods*, *One- and Two-Photon MSIM Data Analysis*). The new version of the analysis software is now available along with the original at http://code.google.com/p/msim/.

1. York AG, et al. (2012) Resolution doubling in live, multicellular organisms via multifocal structured illumination microscopy. *Nat Methods* 9(7):749–754.
2. Nielsen T, Fricke M, Hellweg D, Andresen P (2001) High efficiency beam splitter for multifocal multiphoton microscopy. *J Microsc* 201(Pt 3):368–376.
3. Niesner R, Andresen V, Neumann J, Spiecker H, Gunzer M (2007) The power of single and multibeam two-photon microscopy for high-resolution and high-speed deep tissue and intravital imaging. *Biophys J* 93(7):2519–2529.
4. Fittinghoff DN, Squier JA (2000) Time-decorrelated multifocal array for multiphoton microscopy and micromachining. *Opt Lett* 25(16):1213–1215.
5. Andresen V, et al. (2012) High-resolution intravital microscopy. *PLoS ONE* 7(12): e50915.
6. Bewersdorf J, Pick R, Hell SW (1998) Multifocal multiphoton microscopy. *Opt Lett* 23(9):655–657.
7. Fujita K, et al. (1999) Real-time imaging of two-photon-induced fluorescence with a microlens-array scanner and a regenerative amplifier. *J Microsc* 194(Pt 2-3):528–531.
8. Straub M, Lodemann P, Holroyd P, Jahn R, Hell SW (2000) Live cell imaging by multifocal multiphoton microscopy. *Eur J Cell Biol* 79(10):726–734.
9. Egner A, Hell SW (2000) Time multiplexing and parallelization in multifocal multiphoton microscopy. *J Opt Soc Am A Opt Image Sci Vis* 17(7):1192–1201.
10. Grant DM, et al. (2005) Optically sectioned fluorescence lifetime imaging using a Nipkow disk microscope and a tunable ultrafast continuum excitation source. *Opt Lett* 30(24):3353–3355.
11. Kobayashi M, et al. (2002) Second-harmonic-generation microscope with a microlens array scanner. *Opt Lett* 27(15):1324–1326.
12. Shimozawa T, et al. (2013) Improving spinning disk confocal microscopy by preventing pinhole cross-talk for intravital imaging. *Proc Natl Acad Sci USA* 110(9): 3399–3404.
13. Buist AH, Müller M, Squier J, Brakenhoff GJ (1998) Real time two-photon absorption microscopy using multi point excitation. *J Microsc* 192(2):217–226.
14. Egner A, Jakobs S, Hell SW (2002) Fast 100-nm resolution three-dimensional microscope reveals structural plasticity of mitochondria in live yeast. *Proc Natl Acad Sci USA* 99(6):3370–3375.

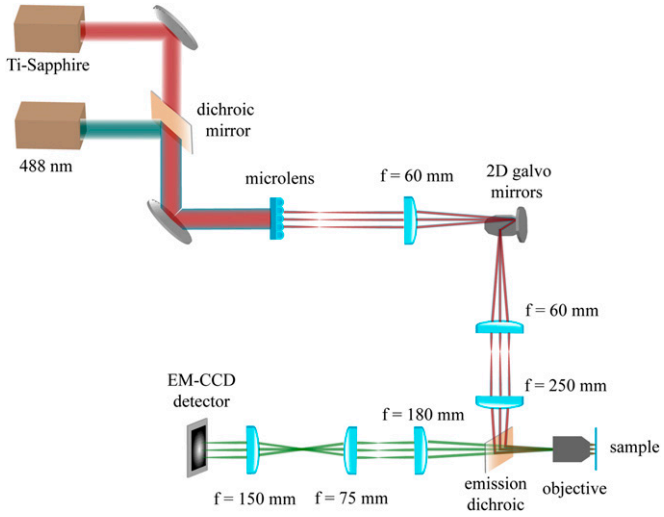

Fig. S1. The Ti:sapphire tunable laser and the 488-nm laser paths are combined using a dichroic mirror and converted into multiple excitation foci using a microlens array. Translation of the excitation foci at the sample plane is achieved by scanning a 2D galvanometric mirror that is conjugate to the objective back focal plane. A tube lens of 250-mm focal length was placed at the right-side port entrance of an Olympus IX-71 widefield microscope. The focal length of this tube lens ensured that the image of the 2D galvo overfilled the back focal plane of the 60× 1.2-numerical aperture (N.A.) water objective, producing diffraction-limited spots at the sample plane. The emission dichroic mirror was custom fabricated by Chroma Technology Corp. to reflect laser beams at 405, 488, 561, 640, and 800–1,100 nm while transmitting emission bands between these lines.

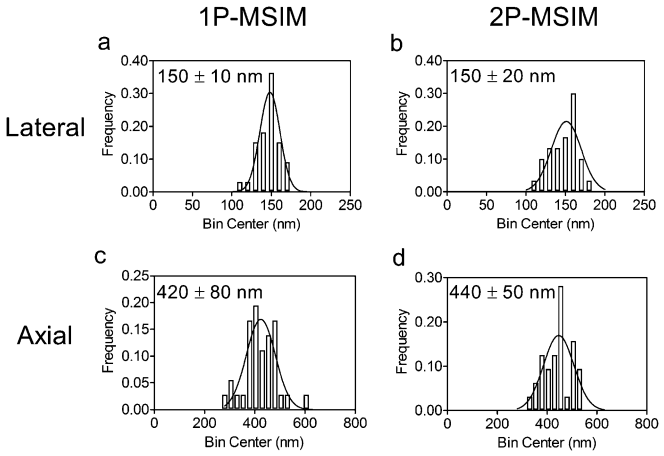

Fig. S2. Full width at half maximum (FWHM) of 0.1-μm fluorescent beads suspended in 3% agarose gel. The average lateral FWHM ± SD is (*A*) 150 ± 10 nm for 488 nm excitation and (*B*) 150 ± 20 nm for 850 nm excitation. The FWHM along the axial direction is (*C*) 420 ± 80 nm for one-photon (1P)-MSIM and (*D*) 440 ± 50 nm for 2P-MSIM. The lateral FWHM was determined by Gaussian fits of line plot profiles from maximum projections of a 5-μm-thick volume imaged at 0.2-μm intervals. At least 30 beads were measured for each case, at 5 μm distance from the coverslip. Imaging was performed with an Olympus point spread function (PSF)-corrected 1.2-N.A. water objective lens.

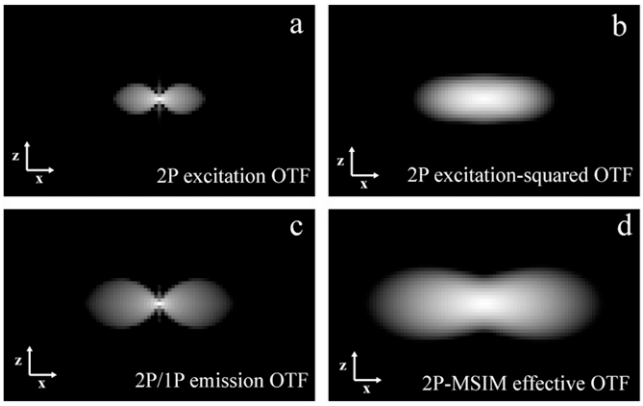

Fig. S3. Simulation of the optical transfer function (OTF) of 2P-MSIM. Logarithms of absolute values of xz slices of each OTF are shown for (*A*) excitation OTF, (*B*) excitation-squared OTF, (*C*) emission OTF, and (*D*) effective 2P-MSIM OTF. Simulations were implemented using Python as described in Dataset S1.

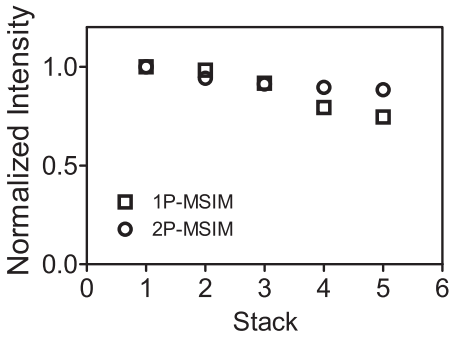

Fig. S4. Power levels for one- and two-photon excitation were chosen to equalize photobleaching in a test sample. Alexa Fluor 488 lamin-C–labeled salivary glands were imaged by acquiring 50-μm stacks at 1-μm interslice separation. The power levels shown in this figure produce equivalent bleaching, and correspond to 6 μW of 488-nm laser power (squares) and 1.1 W of 850-nm, two-photon laser power (circles). Power was measured at the right-side port of the microscope. When the slice number was halved, the power settings for the one-photon laser were doubled. These acquisition settings were used for acquisition on all other samples and have upper limits of ~3.5 W/cm^2 and 5×10^6 W/cm^2 average intensity within the one- or two-photon spots, respectively. The average intensities over the field of view are calculated to have upper limits of ~0.2 W/cm^2 and ~2.9×10^5 W/cm^2 for one- and two-photon illumination, respectively. The two-photon peak intensity is calculated to have an upper limit of ~4.5×10^{11} W/cm^2 within each spot.

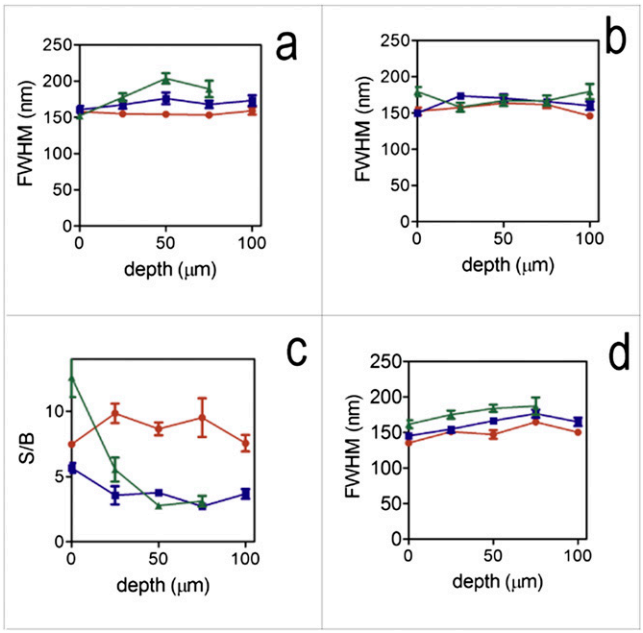

Fig. S5. Yellow-green 0.1-μm fluorescent beads suspended in 3% agarose gel were imaged as a function of depth and scattering. When the laser powers are normalized based on emission intensity using the nonscattering sample, beads are visible with 2P-MSIM whereas very few beads are visible with 1P-MSIM at depths greater than 50 μm. Nevertheless, the FWHM values of the observed beads remain constant. The measurements of FWHM as a function of depth in 0% (red circles), 0.13% (blue squares), or 0.26% (green triangles) nonfluorescent polystyrene beads are shown for (*A*) 1P- and (*B*) 2P-MSIM. Similar results were obtained when the 488 laser power was normalized by photobleaching rate. Again, signal-to-background (S/B) in 1P-MSIM (*C*), as defined by the ratio of the amplitude over offset of a Gaussian fit to 1D plot profiles, decreased with depth in the scattering samples at a greater rate than with 850-nm excitation (Fig. 2*F* in the main text). Although the decrease of S/B when normalizing by the photobleaching rate made it difficult to observe beads at large depths when using one-photon excitation, the FWHM of the beads that were observed displayed little dependence on either imaging depth or the concentration of scattering beads (*D*).

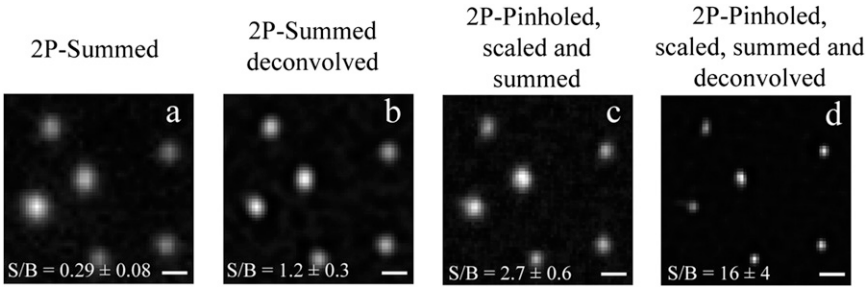

Fig. S6. The bead samples with no extra scattering beads were imaged using two-photon excitation at ~1.8 μm deep. The images were processed by (*A*) summing the images (widefield); (*B*) summing the images before deconvolution (deconvolved widefield); (*C*) pinholing, scaling, and summing the images (MPSS image); and (*D*) pinholing, scaling, summing, and deconvolving the images (MSIM). S/B were determined from the amplitude and offset of Gaussian fits to plot profiles of the bead signals. (Scale bars: 0.5 μm.)

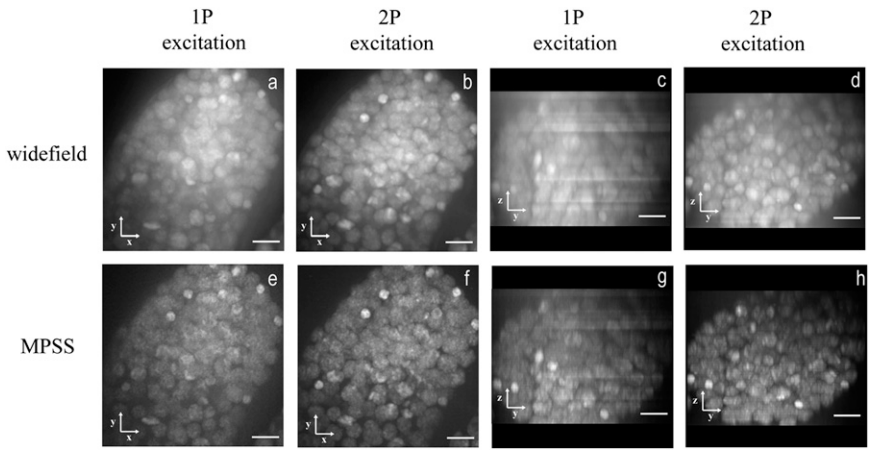

Fig. S7. (*A–D*) Widefield and (*E–H*) MPSS images were collected during imaging of a *Caenorhabditis elegans* embryo expressing H2B-EGFP using 488- or 850-nm excitation. Widefield images were generated by summing the fluorescence from the unprocessed images collected during the (*A* and *C*) 1P- or (*B* and *D*) 2P-MSIM imaging of a 25-μm volume and are shown here as maximum-intensity (*A*, *B*, *E*, and *F*) *XY* and (*C*, *D*, *G*, and *H*) yz projections. (*G* and *H*) yz projections highlight the higher contrast obtained with multiphoton excitation at greater sample depths. (Scale bars: 5 μm.)

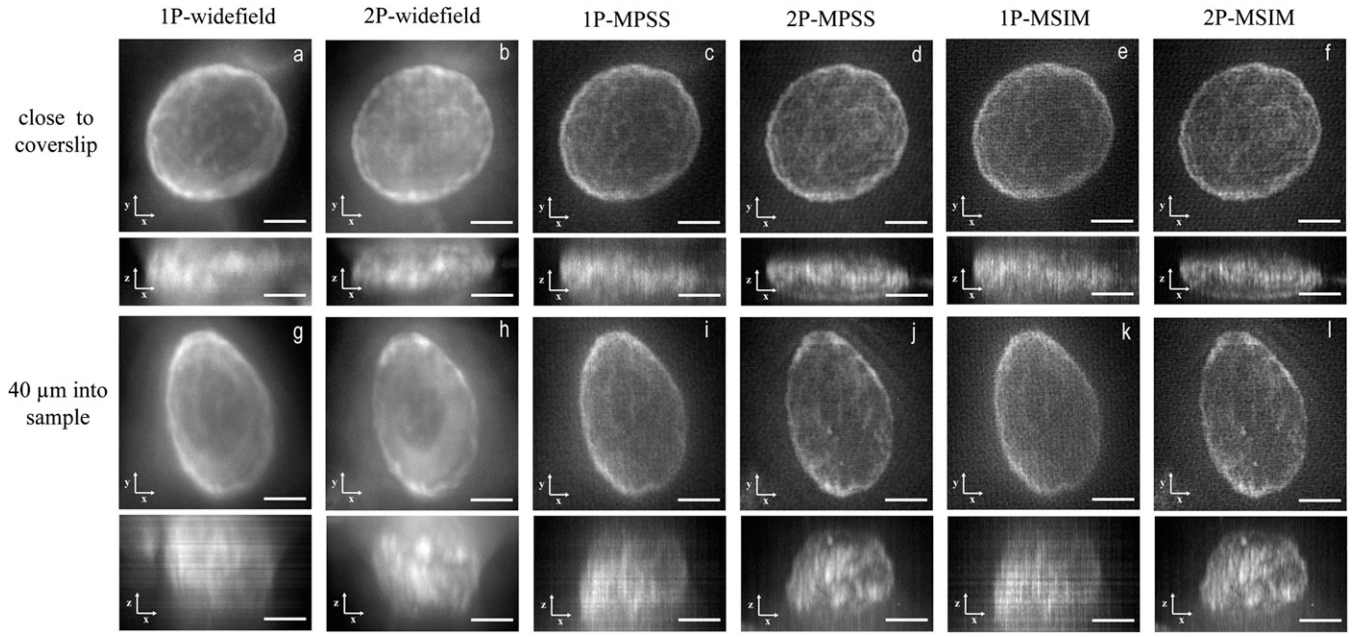

Fig. S8. Imaging of an Alexa Fluor 488 lamin-C–labeled *Drosophila melanogaster* salivary gland using (*A*, *C*, *E*, *G*, *I*, and *K*) 488- or (*B*, *D*, *F*, *H*, *J*, and *L*) 850-nm excitation. Each panel displays maximum-intensity xy and xz projections from a volume sampled at 0.2 μm close to the coverslip (*Upper*) or 40 μm into the sample (*Lower*). *A*, *B*, *G*, and *H* are widefield images; *C*, *D*, *I*, and *J* are pinholed, scaled, and summed images; and *E*, *F*, *K*, and *L* are MSIM images. (Scale bars: 5 μm.)

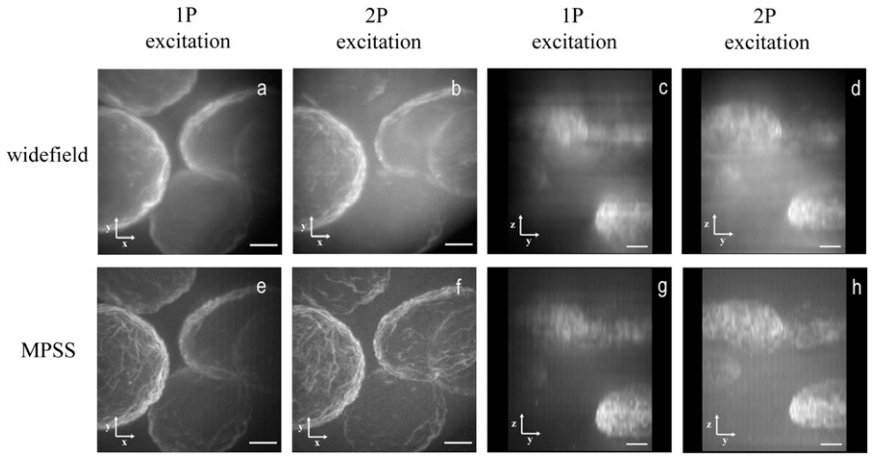

Fig. S9. (*A*–*D*) Widefield and (*E*–*H*) MPSS images were collected by imaging an Alexa Fluor 488 lamin-C–labeled salivary gland using (*A*, *E*, *C*, and *G*) 488- or (*B*, *D*, *F*, and *H*) 850-nm excitation. Widefield images were generated by summing the fluorescence from the unprocessed images collected during (*A* and *C*) 1P- or (*B* and *D*) 2P-MSIM imaging of a 50-μm volume and are shown here as maximum-intensity (*A* and *B*) xy and (*C* and *D*) yz projections. Their corresponding *YZ* projections (*G* and *H*) highlight the higher contrast obtained with multiphoton excitation at greater sample depths. (Scale bars: 5 μm.)

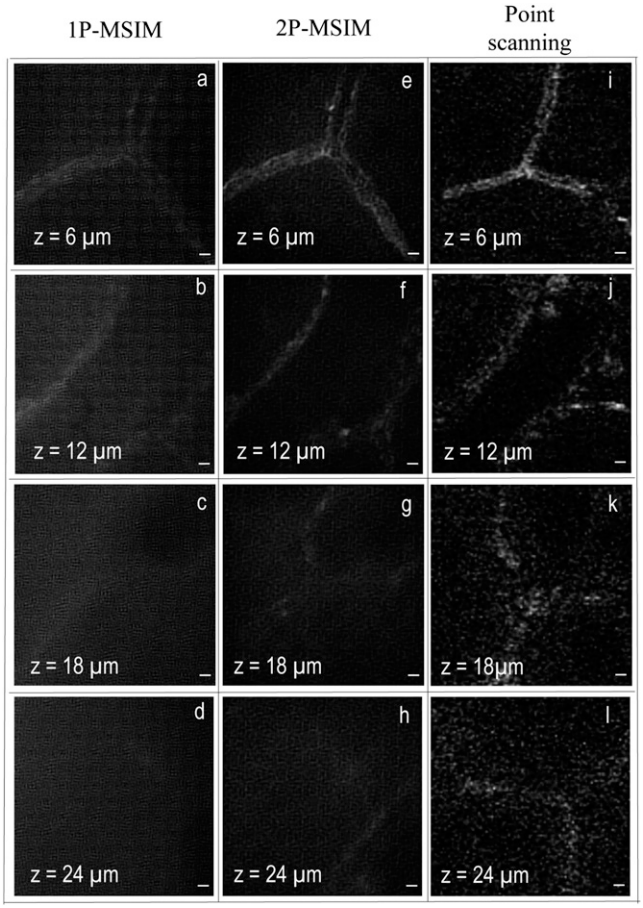

Fig. S10. Millimeter-thick sections of liver from myosin IIA-EGFP transgenic mice were placed on the coverslip and imaged with 1P-MSIM (*A*–*D*), 2P-MSIM (*E*–*H*) , or a point-scanning multiphoton excitation microscope (*I*–*L*) . The images in *I*–*L* are deconvolved similarly to MSIM images, but represent a different field of view and were collected with independently determined acquisition parameters. For the same volumetric photobleaching rate, 2P-MSIM (*E*–*H*) imaged deeper and with higher signal-to-noise ratio than 1P-MSIM (*A*–*D*). In this highly scattering sample, point-scanning two-photon microscopy was able to image deeper (*I*–*L*), but at poor signal-to-noise ratio. (Scale bars: 1 μm.)

Table S1. Apparent size of subdiffractive beads

Excitation	Dimension	Widefield, nm	Widefield deconvolved, nm	MPSS; nm	MSIM, nm
One-photon	Lateral	330 ± 20	240 ± 20	260 ± 20	150 ± 10
	Axial	900 ± 200	600 ± 100	730 ± 100	420 ± 80
Two-photon	Lateral	320 ± 70	270 ± 20	260 ± 20	150 ± 20
	Axial	800 ± 100	590 ± 70	650 ± 70	440 ± 50

Widefield FWHM of 0.1-m fluorescent beads suspended in 3% agarose gel in water, after deconvolution, after MPSS, and after 1P- or 2P-MSIM and deconvolution. The average lateral FWHM ± SD was determined by Gaussian fits of plot profiles of lines on maximum projections of a 5-μm volume imaged at 0.2-μm intervals. At least 10 beads were measured at 5 μm distance from the coverslip. Imaging was performed with an Olympus PSF-corrected 1.2-N.A. water objective lens. MPSS, multifocal-excited, pinholed, scaled, and summed; MSIM, multifocal structured illumination microscopy.

Table S2. Apparent size of immunolabeled microtubules

Excitation	Dimension	Widefield, nm	MPSS; nm	MSIM, nm
One-photon	Lateral	350 ± 40	240 ± 20	150 ± 20
	Axial	900 ± 200	800 ± 100	600 ± 100
Two-photon	Lateral	360 ± 30	260 ± 30	160 ± 20
	Axial	900 ± 100	700 ± 100	500 ± 100

U2OS cells were labeled with an anti-tubulin antibody and an Alexa 488-labeled secondary antibody before mounting in ProLong Widefield, nm. Imaging was performed with a PSF-corrected Olympus 1.2-N.A. water objective lens. The apparent FWHM of microtubules was determined by Gaussian fits of plot profiles of lines which were selected to be approximately orthogonal to the long axis of the microtubule. The mean and SDs are calculated from at least 30 measurements.

Other Supporting Information Files

Dataset S1 (DOC)